2017-12-01

Strain Path Effect on Austenite Transformation and Ductility in Q&P 1180 Steel

Jeffrey Grant Cramer
Brigham Young University

Strain Path Effect on Austenite Transformation and

Ductility in Q&P 1180 Steel

Jeffrey Grant Cramer

A thesis submitted to the faculty of
Brigham Young University
in partial fulfillment of the requirements for the degree of

Master of Science

Michael P. Miles, Chair
David T. Fullwood
Yuri Hovanski

School of Technology

Brigham Young University

ABSTRACT

Strain Path Effect on Austenite Transformation and
Ductility in Q&P 1180 Steel

Jeffrey Grant Cramer
School of Technology, BYU
Master of Science

The ductility of Q&P 1180 steel was studied with regard to retained austenite transformation under different strain paths. Specimens were tested in uniaxial tension in a standard test frame as well as in situ in the scanning electron microscope (SEM). Then digital image correlation (DIC) was used to compute the effective strain at the level of the individual phases in the microstructure. Stretching experiments were also performed using limiting dome height (LDH) tooling, where specimens were strained in both biaxial and plane strain tension. The experiments were done incrementally, for each strain path, and the retained austenite at each level of strain was measured using electron backscatter diffraction (EBSD). Retained austenite levels in the uniaxial tension case dropped from an initial measured level of about 8% to about 2% during an initial strain increment of 0.02, but then stabilized as the specimen was strained to 0.1. In the plane strain and biaxial tension cases retained austenite also dropped significantly during an initial strain increment of about 0.04, but then continued to decrease as the specimens were strained to failure. Biaxial tension, in particular, was the most effective strain path for transforming retained austenite to martensite, resulting in a final volume fraction of 0.3% at an effective strain of 0.3. Retained austenite in the plane-strain tension case dropped at a faster rate than in the biaxial tension case, but finished at about 1% at a strain of 0.1. The greatest limit strains were seen in the biaxial tension case, which may be partly explained by the more effective conversion of retained austenite than was seen in the uniaxial tension case.

ACKNOWLEDGEMENTS

I wish to thank all of my professors at Brigham Young University. Throughout my years here as an undergrad and grad student I have had many opportunities to work with or learn from them. Their willingness to impart their time, knowledge, and expertise has been greatly appreciated.

Without minimizing the important contributions of all my professors, I wish to specifically express my gratitude to Dr. Michael Miles. Between two international internships under his guidance, being his TA, and having him as my advisor I have learned a great deal. Your guidance, help, and encouragement these past few years have been invaluable. Thanks also to Dr. David Fullwood for his EBSD expertise and advisement. I am grateful for the time he spent helping me on this project. Finally, I want to thank Derrik Adams for being a great teammate on this project. We spent a lot of time together and I appreciate his help and his tolerance for my frequent story telling.

TABLE OF CONTENTS

LIST OF TABLES

LIST OF FIGURES

1   INTRODUCTION

1.1   Background

The purpose of this research is to characterize microstructure and ductility of TRIP-assisted steels with electron backscatter diffraction (EBSD) in order to better understand the effect of the austenite – martensite phase transformation on ductility and strength. If microstructures can be identified which improve ductility for a given level of strength, then TRIP steels may be able to replace boron containing press hardening steels in some applications of the auto body structure, resulting in a savings of both time and money.

1.1.1   Advanced High Strength Steels

Advanced High Strength Steels (AHSS) are multi-phase steels consisting of martensite, bainite, and/or retained austenite (RA). AHSS are produced by controlling the cooling rate from the austenite or austenite plus ferrite phase, either on the runout table of the hot mill (for hot rolled products) or in the cooling section of the continuous annealing furnace (for cold rolled and coated products)(K. S. Choi, 2009). AHSS have increasingly been used in the auto industry because of the advantages of weight reduction and increased formability compared to other types of high strength steels (Shaw, 2001). AHSS may be categorized based upon the strength properties, which vary between distributors. The threshold for defining an AHSS is roughly defined as: yield strength > 300 MPa and tensile strength > 600 MPa (Kuziak, 2008).

The AHSS family includes Dual Phase (DP), Complex-Phase (CP), Ferritic-Bainitic (FB), Martensitic (MS), Transformation-Induced Plasticity (TRIP), Hot-Formed (HF), Quenching and Partitioning (Q&P) and Twinning-Induced Plasticity (TWIP). These first and second generation AHSS grades are uniquely qualified to meet the functional performance demands of certain parts. For example, DP and TRIP steels are excellent in the crash zones of the car for their high energy absorption. (WorldAutoSteel, 2017)

1.1.2   TRIP Steels

Transformation induced plasticity (TRIP) steels are one of the newest AHSS that the automotive industry has begun working with because of its good combination of strength and ductility. TRIP gain their formability from the transformation of retained austenite into martensite, (known as the TRIP effect), during deformation. A variant of TRIP, the Q&P steels good ductility is attributed to TRIP-assisted behavior of retained austenite during deformation.(De Moor, 2008). Understanding the evolution of the volume faction of retained austenite as the steel is deformed helps us understand the forming limits of the material and how best to use it in production.

Much of the prior work on TRIP steels has focused on the effect of austenite transformation on room temperature ductility, via mechanical testing and evaluation of microstructure. More recently, DIC methods have been applied to the study of TRIP steels, where specimens are strained in situ and microstructure evolution is observed (Di Gioacchino, 2013). EBSD has also been employed in order to better track the transformation of austenite during progressive straining of an in situ specimen. In the present work, both DIC and EBSD were used to study the microstructure of steels containing retained austenite, in order to

understand how the transformation of this phase can impact ductility for several different strain paths.

1.1.3   Quenching and Partitioning Steels

Currently the steel industry is developing the third generation AHSS with the goal of attaining the mechanical properties regime between first and second generation of AHSS at cost slightly higher compared to first generation (Grajcar, 2012). Q&P steels are part of this third generation.

The process to create Q&P steel consists in quenching from the austenite region to below the martensite start temperature, followed by a partitioning treatment to enrich the remaining austenite with carbon, thereby stabilizing it to room temperature (John G Speer, 2005). The fact that carbon has migrated from the martensite to surrounding austenite phases also reduces the relative hardness between the phases and will improve the ability of the material to distribute strain more effectively at the level of the microstructure.

1.1.4   Plastic Strain Mapping with Digital Image Correlation (DIC)

DIC is an image analysis method that can determine strain patterns on the surface of objects under load. This method has been used to study, quantitatively, the plastic deformation at the level of the microstructure, such as in the case of stainless steel (Di Gioacchino, 2013). DIC image analysis relies on a random pattern on the surface in order to track changes in the pattern between images taken at different strain levels. Sometimes an etched microstructure can be used as the pattern, but in other cases sufficient resolution can only be obtained when an artificial speckle pattern is applied to the surface of interest. A new approach that was tried during the course of this research is the use of a forescatter detector (FSD), which can provide high-contrast

images of an unetched specimen during an EBSD scan. This would provide the advantage of having a good correlation between the strain pattern from DIC and the underlying microstructure data emerging from analysis of the EBSD data.

1.1.5   Forming Limit Diagram

The forming limit diagram (FLD) is used in a practical manner to help engineers predict when the strain levels in a complex stamping are in the danger zone and apt to provoke a split failure during production. The FLD is generated experimentally by straining sheets under different strain paths, while simultaneously using circle grid analysis or DIC to measure surface strains until failure. The strains that occur just prior to necking are termed "limit" strains. The locus of points generated by many experimental measurements, under different strain paths, create a boundary above which a sheet would be expected to fail, and below which the sheet would be expected to be safe (Handbook, 2006). In this research project, the limit strains in Q&P 1180 steel sheet were measured and plotted on a graph of major strain versus minor strain, thus generating an FLD.

1.2   Hypotheses

The primary hypotheses to be tested during this research project are as follows, relating to a Q&P 1180 sheet alloy:

1. Conversion of retained austenite to martensite will be dependent on plastic strain level, and will be a non-linear function of strain.

2. Conversion of retained austenite to martensite will be dependent on strain path, where greater levels of restraint in forming boundary conditions will result in greater conversion of retained austenite.

1.3 Delimitations

This research was focused on characterizing Q&P 1180 sheet steel. Other similar alloys have different phase morphologies, which could be compared and contrasted to the behavior of the current alloy. But this research did not explore or evaluate other AHSS.

1.4 Definitions of Terms

AHSS – Advanced High Strength Steel. Steels that have an ultimate tensile strength of 550 MPa or above are considered AHSSS

TRIP steel – Transformation induced plasticity Steel

RA – Retained Austenite

Q&P 1180 – A TRIP steel with an ultimate strength of 1180 MPa or 171 ksi.

DIC – Digital image correlation

EBSD – Electron backscatter diffraction

FLD – Forming Limit Diagram

FIB – Focused Ion Beam

SEM – Scanning electron microscope is a type of electron microscope that produces images of a sample by scanning it with a focused beam of electrons.

Wire EDM– Electrical discharge machining is a manufacturing process in which electrical discharges are used to cut out desired shapes

UTS – Ultimate Tensile Strength is the capacity of a material or structure to withstand loads

tending to elongate

.

2 LITERATURE REVIEW

2.1 Introduction

The drive to manufacture cars with better fuel efficiency has long been a difficult technical problem for the auto industry, but especially in the last decade as more regulations are put into place mandating certain standards. The use of advanced high strength steels (AHSS) has increased within the automotive industry in order to meet these regulations. Transformation induced plasticity steels (TRIP) are one of the newest AHSS the automotive industry has begun working with because of its good combination of strength and ductility. This is a major advantage of TRIP steels because it allows them to be used to form more complex parts than typical AHSS (Kwon, 2010).

2.2 Advanced High Strength Steels

With increasing mandates and requirements for passenger safety, vehicle performance and fuel economy, the steel industry has increased development of AHSS. However, AHSS formability is not sufficient to form the complex shapes that are needed for some parts of the body-in-white (BIW) structure. Over the past 20 years, steel alloys have undergone a great deal of research and development especially in obtaining a good balance of strength and formability (Kuziak, 2008).
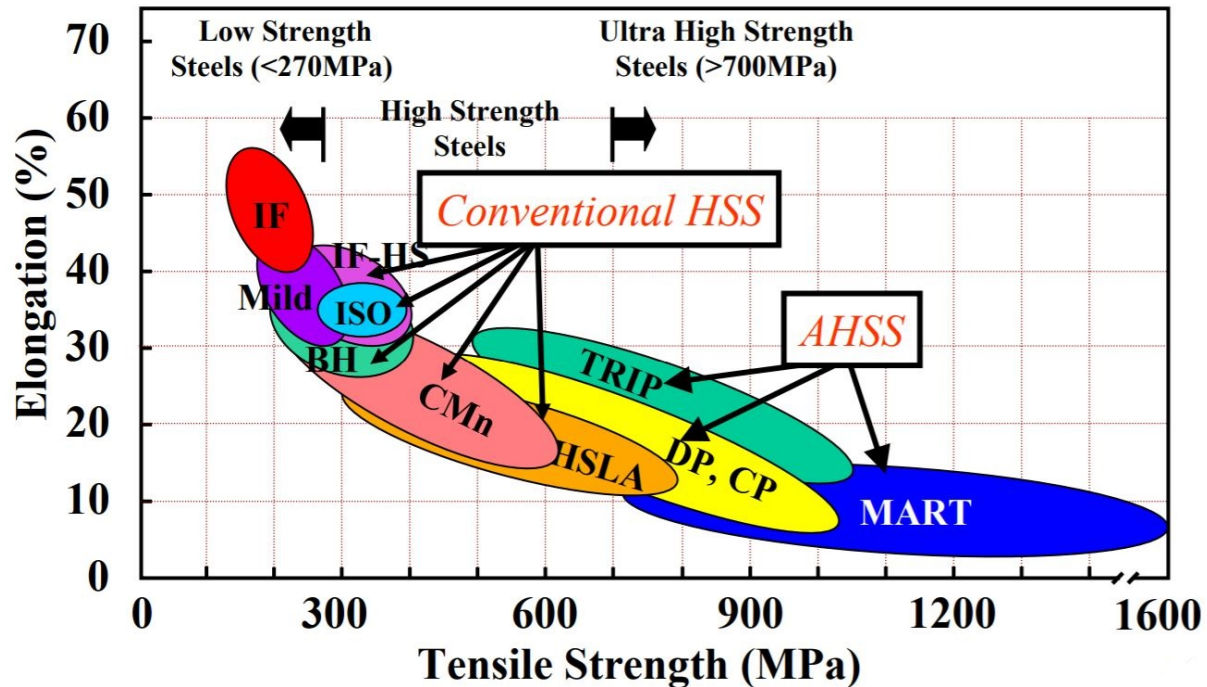
Fig 1-Total Elongation (%EL) vs. Ultimate Tensile Strength (UTS)

These steels are characterized by improved formability and crash worthiness compared to conventional steel grades. A comparison of conventional steels and AHSS can be seen in Figure 1 (Shaw, 2001). First generation and second generation of AHSS consists of dual phase steels, complex phase steels, and TRIP steels.

2.2.1 TRIP Steels

Bainitic steels were developed in order to attain a good combination of strength and ductility, beyond what was possible with DP steels. These alloys have a smaller contrast in hardness between the various phases present in the microstructure than is true with DP steels (S. H. Choi, 2014; Sadagopan, 2003). When retained austenite is combined with bainite, ferrite, and some martensite the resulting material is referred to as transformation induced plasticity (TRIP) steel, where the volume fraction of retained austenite can reach 20% (Grajcar, 2012). Lower alloy

versions of this material are called TRIP-aided bainitic ferritic (TBF) steel if the retained austenite portion of the microstructure is smaller, usually about 10% or less (Bhadeshia, 2002). TBF steels have slightly more carbon and significantly more silicon than DP steels. The higher silicon content is needed to minimize the formation of cementite during the transformation of austenite to bainite (Krauss, 2015). Chemistry and thermomechanical processing give TBF steels a microstructure composed of bainitic-ferrite laths, with finely dispersed retained austenite in between the laths (Miura, 2008). When TBF steel is deformed plastically, much of the retained austenite transforms to martensite, thereby increasing the hardening rate and overall formability of these alloys, compared to DP steels having similar levels of tensile strength. In addition to the beneficial effect of austenite transformation to martensite, TBF steel ductility is increased because the tendency for strain localization around hard phases in the microstructure is lower than for DP steel, where its ability distribute strain across different phases in the microstructure is greater. The TBF alloys have a little more ductility than equivalent DP steels, as measured by total elongation in a tension test, and they also have a higher work hardening rate. For example, TBF 980 has a strain hardening exponent (n) of 0.22, versus 0.15 for DP 980 (Kimura, 2011). Higher n correlates to better strain distribution in a press forming operation, where complex strain paths are typical.

The volume fraction of retained austenite in the final microstructure is mostly determined by the amount of silicon and carbon content of the TRIP steel. AHSS such as dual phase (DP) and TRIP steels are being increasingly used in the automotive industry because they exhibit higher strength and ductility compared to other high strength steels (Kwon, 2010). Research and Development on these steels have been mainly focusing on how to utilize the microstructure containing the phase transformation products such as retained austenite. Strain mapping using

9

Micro DIC and electron backscatter diffraction (EBSD) allows us to better understand the microstructure of these steels.

2.2.2   Quenching and Partitioning Steels

Q&P steels show promise as a third Gen AHSS because they maintain a high amount of retained austenite (RA) through a unique process. This process begins with the complete austenitization of the steel. It then proceeds with the quenching of the steel below the martensite start (Ms) temperature but above the martensite finish (Mf) temperature. A final step of partitioning the carbon from the supersaturated martensite to the remaining austenite by either keeping it at the quench temperature (one-step) or raising the temperature slightly (two-step) is then taken (Edmonds, 2006), (Clarke, 2008), and (J. G. Speer, 2014). "The microstructure of commercial Q&P steels is composed primarily of martensite (50–80%) formed during quenching, and ferrite (20–40%) formed from the austenite phase during slow cooling, as well as dispersed retained austenite (5–10%) stabilized by carbon enrichment during partitioning."(Wang, 2013) The increased amount of carbon in the retained austenite allows it to remain when the metal is then cooled to room temperature (Santofimia, 2011). This high amount of metastable retained austenite, which transforms to martensite when adequately strained, contributes significantly to the resulting metal's transformation induced plasticity (TRIP) effect. This effect allows it to have both the necessary high strength and high ductility properties that contribute to its ability to be formed. While this is not a new concept, as TRIP steels have been around for several decades (Blondé, 2012), the fact that the Q&P process can produce these types of metals at a reduced cost is quite promising (de Diego-Calderón, 2016).Various microstructures, and hence mechanical properties, can be obtained by varying the parameters. (De Knijf, 2015) "Evolution of the volume fraction of retained austenite is generally divided into

two stages: a rapid decrease at low strains (stage I) and more sluggish decrease at high strains (stage II). Retained austenite is distributed both as thin films and as larger blocky regimes. It is clear that the retained austenite fraction decreases with increased strain, and the remaining austenite particles are mostly the finer ones" (Wang, 2013).

Table 1 Composition of Q&P 1180

Supplier	Grade	C	Mn	Si	Cr	Mo	Ni	Ti	AL	Nb	V	B	Cu	S	P
BAO	1180 Q&P - Uncoated	0.19	2.8	1.6	0.01	0.002	0.008	0.004	0.04	<.001	0.002	0.0003	0.01	0.001	0.006

2.3 Plastic Strain Mapping with Digital Image Correlation

Digital Image Correlation (DIC) is an image analysis method that can determine surface strain maps of objects under load. DIC measures the shifts in patterns that are printed onto the surface of the objective to be studied. The changes in the pattern are used to determine surface strains. When applied to images from the scanning electron microscope (SEM) this method has been used to study, quantitatively, the plastic deformation at the microstructural scale of polycrystalline materials.(Di Gioacchino, 2013). Understanding the deformation mechanisms in polycrystalline materials, it is necessary to observe the microstructure in situ during stretching of the material.

2.4 Forming Limit Diagram

The forming limit diagram (FLD) is used in a practical manner to help engineers predict when the strain levels in a complex stamping are in the danger zone and apt to provoke a split failure during production. The FLD is generated experimentally by straining sheets under different strain paths, while simultaneously using circle grid analysis or DIC to measure surface

11

strains until fracture. The strains that occur just prior to fracture are termed "limit" strains. The locus of points generated by many experimental measurements, under different strain paths, create a boundary above which a sheet would be expected to fail, and below which the sheet would be expected to be safe (Handbook, 2006). In this research project, the limit strains on TRIP assisted steel sheet were measured and plotted on a graph of major strain versus minor strain, thus generating an FLD. Specimens were subsequently stretched to different strain levels along three different strain paths: uniaxial tension, plane strain tension, and biaxial tension. Portions of each specimen were cut, mounted, and polished in order to perform EBSD scans on the strained material. Levels of retained austenite were calculated from scan data for each strain level and strain path, in order to determine whether strain path has an effect on austenite transformation, all other things equal.

3 RESEARCH METHODOLOGY

3.1 Sample Prep and Polishing Micro-Tensile Test Specimens

The material evaluated was 1.25 mm Q & P 1180 steel provided by industrial partner

General Motors R&D. Dog-bone-shape micro-tensile test specimens were cut out using a wire

EDM keeping the tensile axis parallel to the rolling direction. The mini tensile specimens were

polished on one side so that scans could be done in situ. The tensile stage had a load limit of

about 800 N, so in addition to polishing for microscopy the specimens had to be reduced in

thickness to about 0.4 mm to stay under the load limit during plastic straining. Specimen

thickness was reduced by mounting specimens onto steel pucks in order to maintain an even
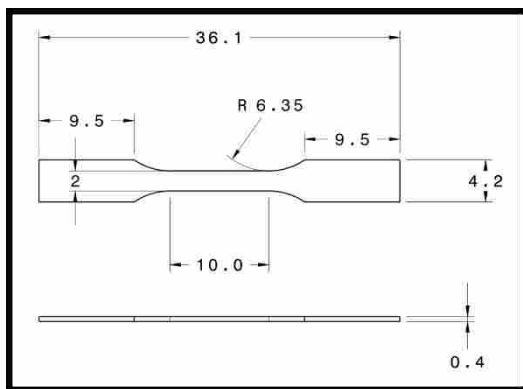
thickness during grinding.

Fig 2-Dimensions of Micro-Tensile Specimens   Fig 3-Specimens Mounted on Steel Pucks

Specimens were first ground down to 0.45 mm thickness using 240 grit paper, and then polished in the following order: grits 400, 600, 800, 1200, and 1200 fine. The specimens were removed from the metal pucks and electropolished using freshly prepared electrolyte with a composition of 25 ml perchloric acid and 75 ml butanol in 125 ml methanol at 20 V and 10 °C for 20 seconds.

3.2   Marking Samples

Specimens were marked with an array of points using a focused ion beam (FIB) to distinguish between samples, to better locate areas of interest, and to return to the same location after each tensile pull. The FIB'd array is made with 400 micron spacing and a variety of patterns to quickly orient in the microscope (Figure 4) and to easily return to the same area after each tensile pull. The FIB'd areas are also used to line up each scan after every pull as seen in Figure 5. This allows for better tracking in DIC software and to track the transformation as the specimen is being pulled.
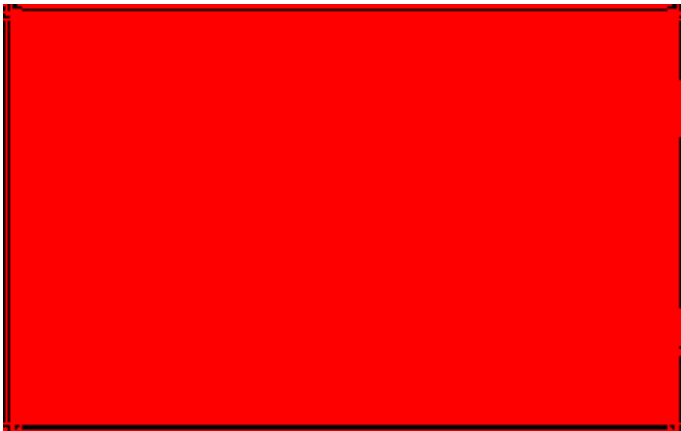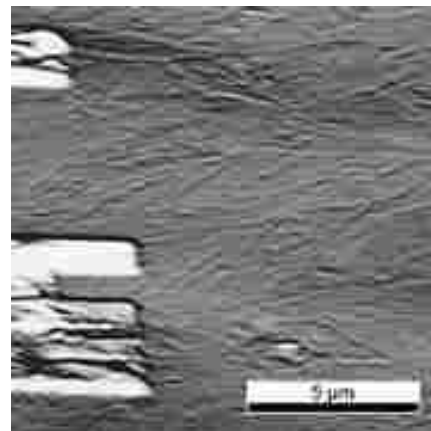

Fig 4-FIB'd Pattern With "#" Replaced With Sample #   Fig 5-FSD Image of FIB'd Area

3.3   EBSD and Images of Micro-Tensile Test Specimens

After samples had been properly polished, they were painted with silver paint, a conductive medium, which helps in obtaining better EBSD scans and FSD images. The samples were then placed in the clamps of the stage of Sandia design (Figure 7) and securely fastened, making sure that the gauge length was properly centered (Figure 6).

After securing the specimen in the stage, areas of interest were scanned after repeated interrupted tensile pulls, thus allowing for images to be obtained at each strain increment. FSD images and EBSD scans were performed on unetched specimens, in order to correlate microstructure-level strains to fractions of austenite transformation, at each level of specimen

Fig 6-Micro-Tensile Specimen in the in situ Stage   Fig 7-in situ Stage of Sandia Design

strain. The EBSD data were acquired on a square scan grid using an accelerating voltage of 20 kV, a working distance of 17 mm, tilt angle of 60 (with 10-degree tilt built into the clamps on the stage) at a magnification of 8000X, a scan size of 17.5x17.5 μm^2, and a step size of 80 nm. Scanning the same area over and over again causes carbon deposition and decreases the quality of the scans which limits the number scans to 4 or 5 in each area.

When diffraction patterns are indexed there can be several possible orientations which match the diffraction bands in the pattern. OIM analysis software ranks these orientations (or

solutions) using a voting scheme. The confidence index value is then based on the results of this voting scheme and ranges from 0 to 1, where 0 represents no votes for an orientation and 1 represents 100% of the votes. In a sample study done by OIM, it was found that 99.5% of the points in a steel with both ferrite (bcc) and austenite (fcc) phases were indexed correctly when the confidence index was only 0.10 (OIM, 2016)

With each consecutive scan, carbon deposition by the beam increased. This increase in carbon buildup decreased the quality of the scan and caused the number of mis-indexed patterns to increase. Since the resulting noise was indexed as austenite, an artificial increase in the amount of austenite was reported, which was contrary to the expected decrease in austenite as it transformed with increasing strain. Therefore, in order to eliminate patterns that were mis-indexed, scans were cleaned using OIM Analysis software to simply remove patterns with a confidence index less than 0.05.

3.4 DIC Image Processing of Micro-Tensile Test Specimens

FSD images were taken using the forescatter detector on the S-Feg XL30 FEI but also created using EDAX Prias software that uses the phosphor screen as a forescatter detector. FSD images were processed using Ncorr, an open source DIC software to generate strain maps (Blaber, 2015). EBSD scans were processed by EDAX OIM software to understand the material's crystallography and how it changes as the material is strained under different conditions. The strain maps and EBSD scans were then compared to evaluate how the microstructure affects material ductility.

Furthermore, a manually DIC procedure was implemented based upon the positional measurement of several pairs of features in the microscope image at each scan step. The result of

this verification process for the sample strain level was to determine that the actual sample strain lagged behind the assumed macroscopic strain due to slippage of the sample in the grips on the first strain step. Subsequent strain increases approximately followed the assumed macroscopic strain step. The reported values of macroscopic strain in the subsequent sections are therefore an overestimate of local strain, but a reasonable estimate of strain increments after the initial step.

3.5   Sample Prep and Polishing FLD Samples

In order to create the forming limit diagram biaxial, plane strain, and tensile tests were performed on specimens of normal size (ie. blanks of the order of 200mm per side for the press forming, and tensile specimens of the order of 200mm long). An Interlaken hydraulic press was used for plane strain and biaxial tension experiments, with standard limiting dome height (LDH) tooling, including a 100mm diameter punch. The press had a maximum clamp load of 334kN and maximum punch load of 223 kN. Tooling with small lockbeads was used to restrain the blanks, where the beads were small enough to prevent breaking the sheet, but large enough to provide restraint, as seen in Figure 8.

Fig 8-Tooling Used for Plane Strain and Biaxial Tension Experiments

Strain was measured by coating the surface of each specimen with a white paint suited for bonding to bare metal. Black paint was then applied to the specimen surface to give a random speckled pattern. An Aramis Digital Image Correlation (DIC) (Systems, 2011) system was used to measure the surface strains during testing.

For biaxial tension, sheets that were 200mmx200mm were used to create a fully clamped specimen. For the plane strain specimens, the standard procedure of testing different blank widths (Figure 9) and plotting punch failure height versus width was performed, with the width corresponding to the minimum height being chosen. This is to determine the conditions that result in a plane-strain fracture, in this case, the width that provided a plane strain fracture was 70mm.
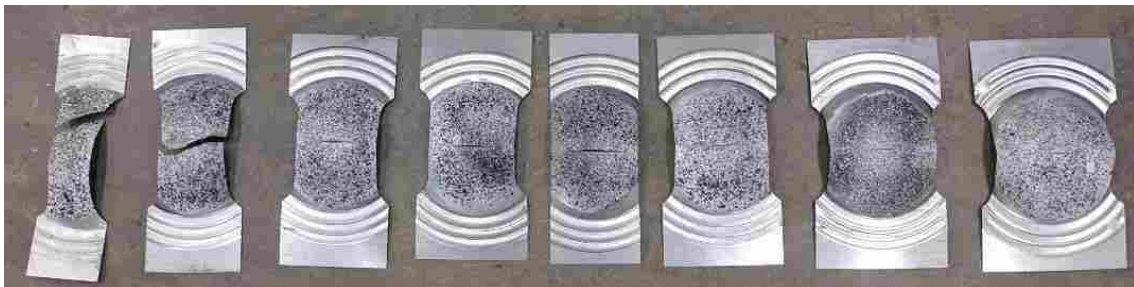

Fig 9-Samples With Different Widths to Determine Plane Strain Condition

Sheets were strained to fracture in uniaxial tension, plane strain tension, and biaxial tension. Then the displacement that resulted in fracture in each case was used to compute incremental displacements of 25%, 50%, and 75% to fracture (in terms of displacement boundary condition, not strain) for each strain path. Then specimens were cut from each sheet and mounted in bakelite, where the rolling direction (RD), transverse direction (TD), and normal direction (ND) of the sheet were represented (three small portions of the sheet cut from the appropriate location), as seen in Figure 11. The bakelite specimens were polished in the

following order: grits 240, 400, 600, 800, 1200, 3 micron diamond paste, and 1 micron diamond paste. The specimens were then put in a vibramat polisher with 0.04 micron colloidal silica for two hours.
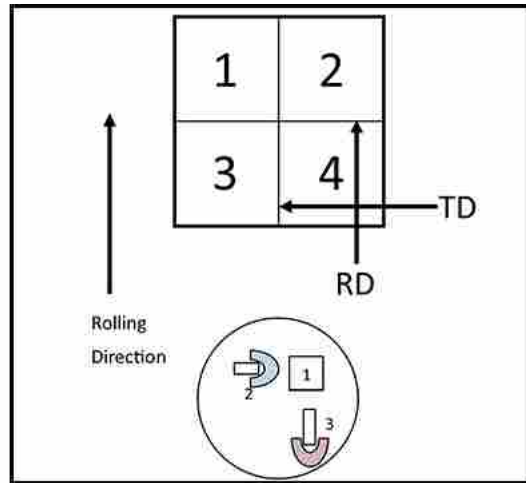

Fig 10-Biaxial Specimen Strained to Fracture   Fig 11-Diagram of Samples Mounted in Bakelite

3.6   EBSD Images of FLD Samples

After FLD samples were mounted and polished, they were painted with silver paint, a conductive medium, which helps in obtaining better EBSD scans. The EBSD data were acquired on a square scan grid using an accelerating voltage of 20 kV, a working distance of 17 mm, tilt angle of 70 at a magnification of 6500X, a scan size of 25x25 μm^2, and a step size of 80 nm. Samples were scanned to determine the percentage of austenite at each level of failure.

4   RESEARCH RESULTS AND DISCUSSION

4.1   Uniaxial Tension Results

The sheet material to be evaluated was 1.25mm Q&P 1180 steel, produced by Baosteel (and provided by General Motors). Tension testing of this material provided an approximate yield strength of 1000 MPa and ultimate tensile strength of 1180-1220 MPa. Total elongations averaged about 15% for three tension tests. Engineering stress-strain curves for this material are shown in Figure 12. An extensometer was not used, so elongation is approximate. Full size ASTM E8 specimens were employed.
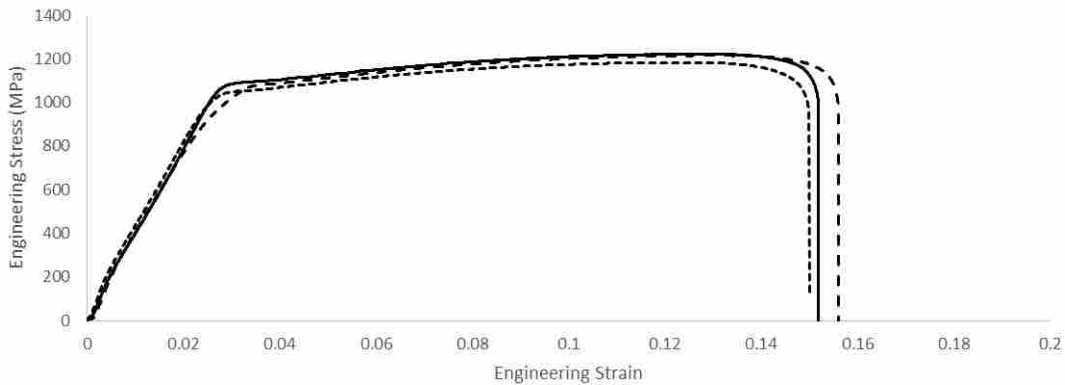

Fig 12-Tension Testing Results for 1.25mm Thick Q&P 1180 Steel

4.1.1　Scan Images & Cleanup

With each consecutive scan, carbon deposition by the beam increased. This increase in carbon buildup decreased the quality of the scan and caused the number of mis-indexed patterns to increase. Since the resulting noise was indexed as austenite, an artificial increase in the amount of austenite was reported, which was contrary to the expected decrease in austenite as it transformed. Therefore, in order to eliminate patterns that were mis-indexed, scans were cleaned using OIM Analysis software to simply remove patterns with a confidence index less than 0.05. Table 2 shows the results of this procedure.

This procedure removes the small pixelated dispersion of 'austenite' that appears due to mis-indexing of the EBSD data as the strain increases, and results in a consistent reduction in austenite percentage with strain, as can be seen in the following sets of images. Further confirmation that the carbon buildup is causing this noisy data is achieved by repolishing the samples, as discussed in the subsequent section.

An additional source of uncertainty in the percentage of austenite within the sample comes from potential transformation of the austenite during the application of fiducial markers using a focused ion beam. This is also discussed in the next section.

Table 2 RA % at Different Strain Levels With & Without Confidence Index Cleanup

	True Strain	No clean up austenite %	CI > .05 Total Fraction austenite %
EP 5 Area 1 0.0	0.0	7.3	4.7
EP 5 Area 1 0.4	0.039	6.8	3.6
EP 5 Area 1 0.6	0.058	7.4	3.4
EP 5 Area 1 0.8	0.077	7.9	2.4
EP 5 Area 1 1.0	0.095	9.8	2.1
EP 5 Area 1 1.2	0.113	11.9	2.3

4.2   In situ Tensile Testing

From the resulting EBSD scans and corresponding amounts of RA at each strain level, it is apparent that the austenite is indeed transforming as the sample is strained. This transformation can be seen in the phase maps in Figure 14-19 (red is austenite and green is ferrite/martensite) as the austenite grains decrease in size or disappear entirely. As expected, the image quality decreases in the regions where the austenite transforms. Such a decrease in IQ can be attributed to the formation of martensite, which is notorious for having poor image quality due to a large amount of dislocations. In Figure 13 show phase maps at 6% strain (left image) and 8% strain (right image) overlaid on Image Quality maps with several austenite grains highlighted. Notice the austenite grains diminishing in size and the resulting image quality being lower after apparent transformation. Additionally, from the graphs in Figure 20 of both Instron and in situ results, it can be seen that most of the austenite transformation occurs in the first 4% of strain, and begins to level off at higher strains.
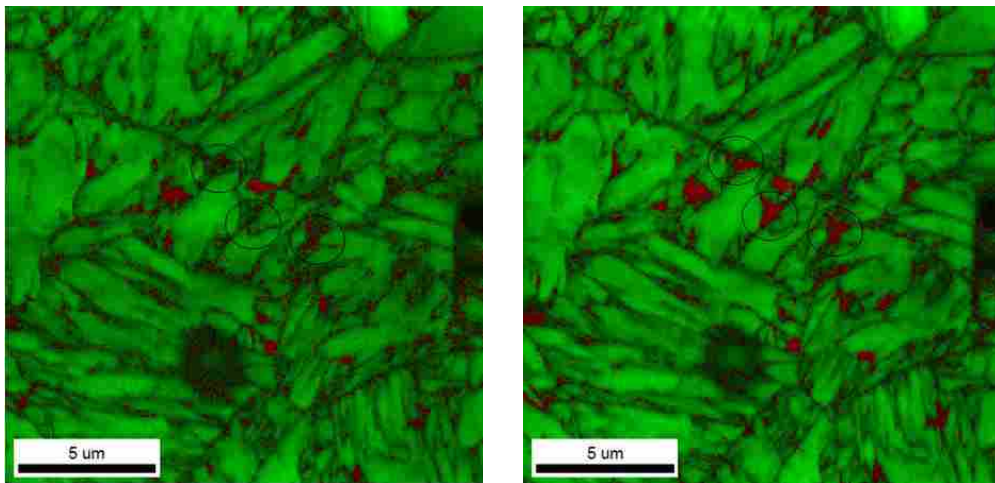

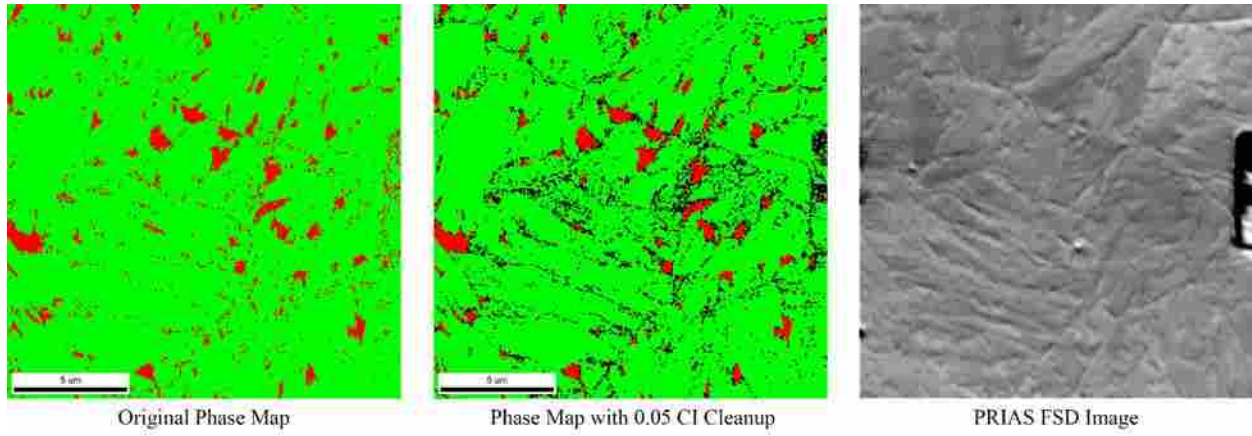Fig 13-Phase Map Overlaid on Image Quality Map at 6% and 8% Strain

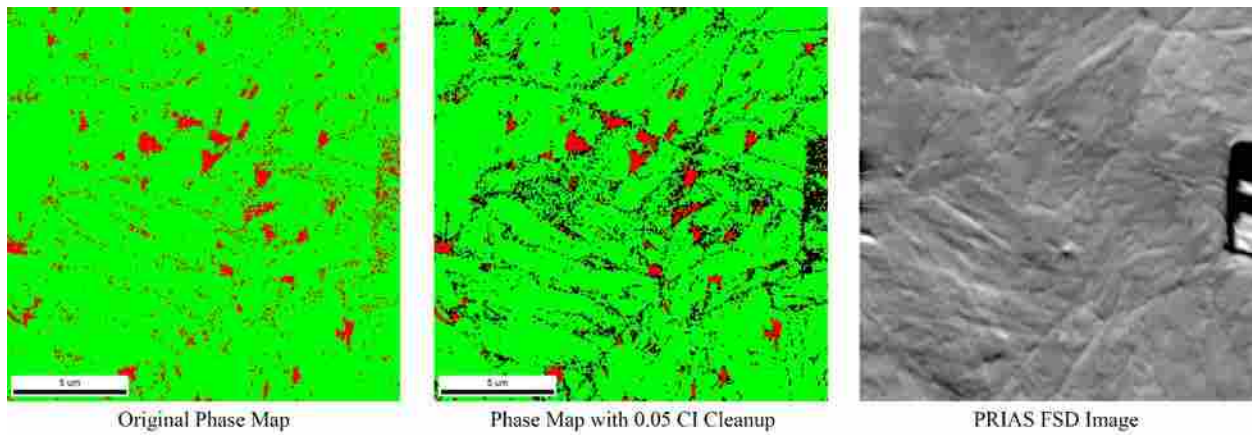Fig 14-Phase Maps and PRIAS FSD Image for 0% Macro Strain

Fig 15-Phase Maps and PRIAS FSD Image for 4% Macro Strain
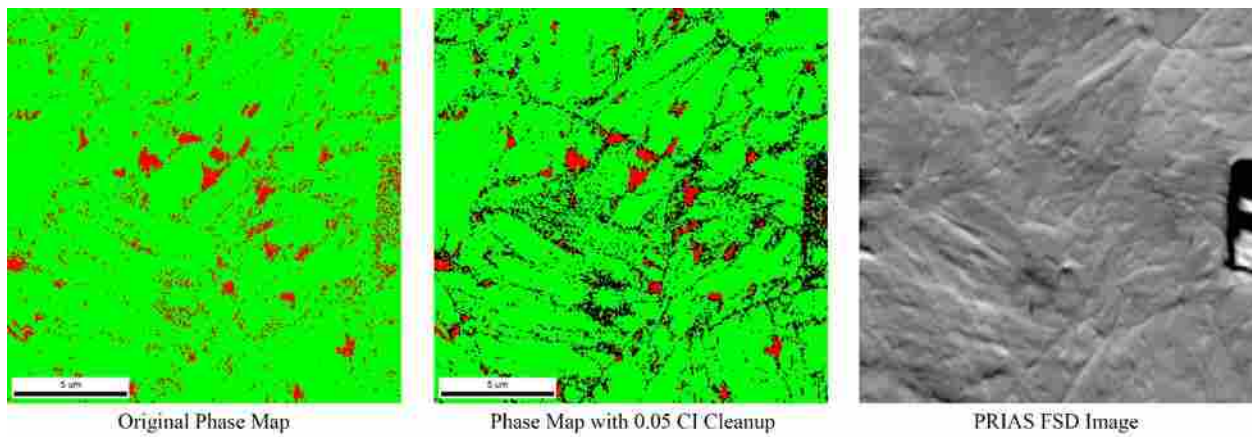
Fig 16-Phase Maps and PRIAS FSD Image for 6% Macro Strain

Original Phase Map   Phase Map with 0.05 CI Cleanup   PRIAS FSD Image
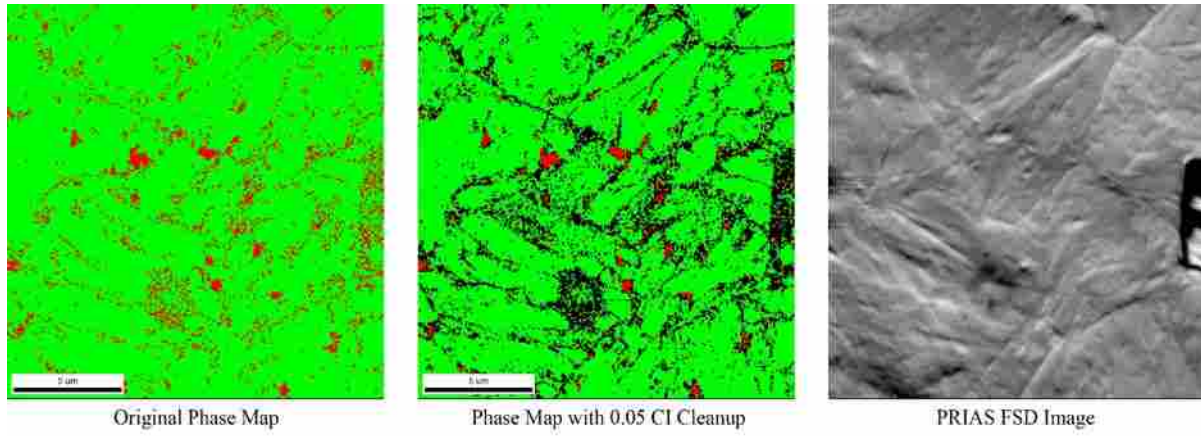
Fig 17-Phase Maps and PRIAS FSD Image for 8% Macro Strain

Original Phase Map   Phase Map with 0.05 CI Cleanup   PRIAS FSD Image
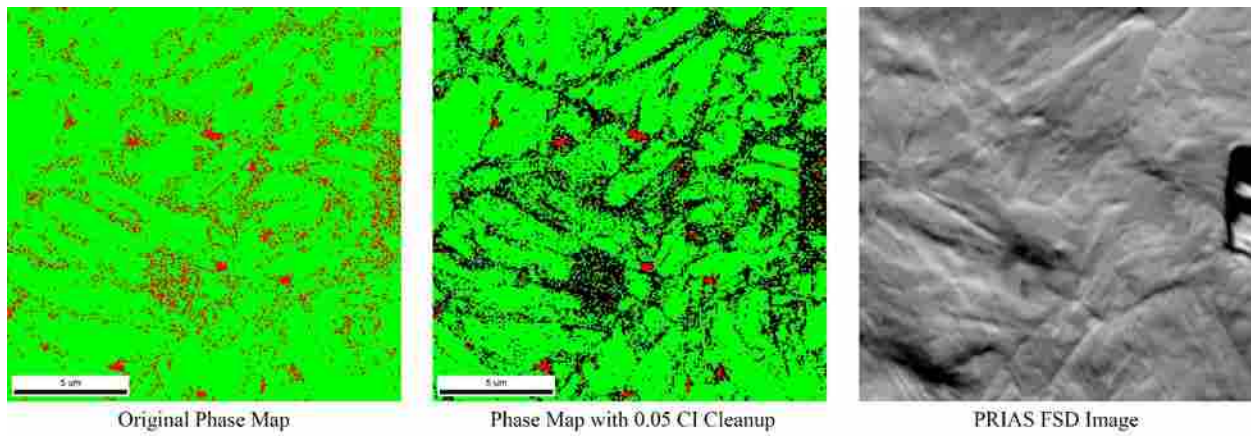
Fig 18-Phase Maps and PRIAS FSD Image for 10% Macro Strain

Original Phase Map   Phase Map with 0.05 CI Cleanup   PRIAS FSD Image
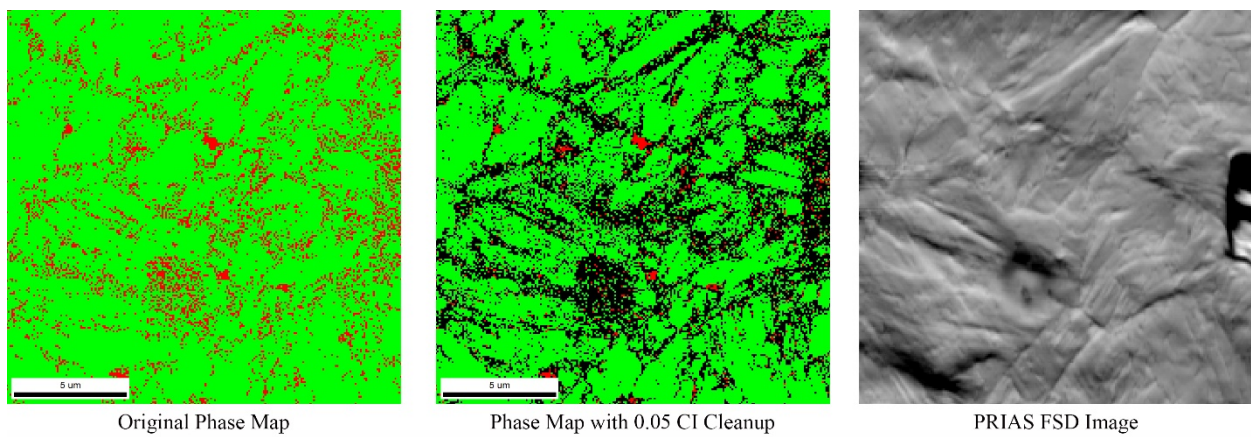
Fig 19-Phase Maps and PRIAS FSD Image for 12% Macro Strain

The results obtained in this study can also be compared to previous results obtained by Wang and Speer for austenite percentage at different levels of strain (Wang, 2013). Figure 20 compares their room temperature results for Q&P 980 with the results from this study.
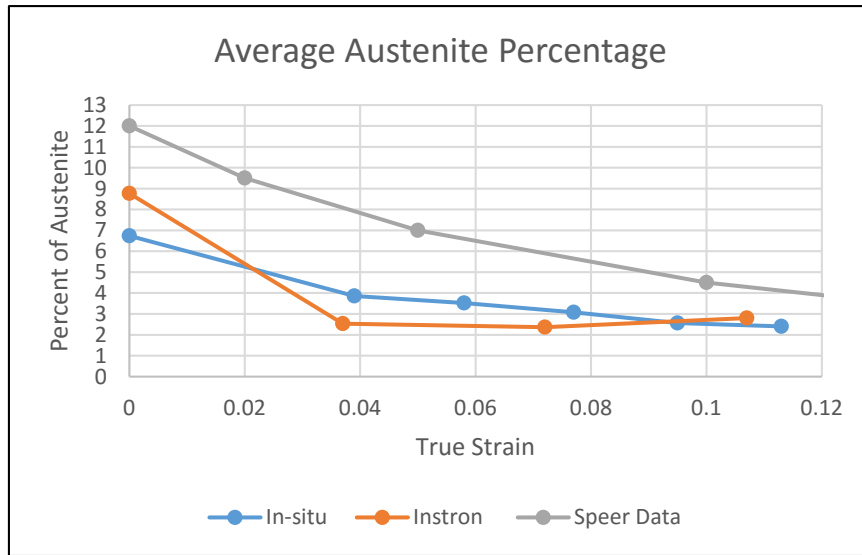

Fig 20 Average RA % for Q&P 1180 in in situ, Instron, & Speer Data (Q&P 980)

With regard to the initial amount of RA for both in situ and ex-situ tensile tests, it is important to note that the values reported via EBSD were far below the expected amount of approximately 15-20%. There are a few possible explanations for this discrepancy. First, the RA content in the Wang and Speer study was found using XRD, which tends to be more precise for phase identification than EBSD (Cakmak, 2015; De Knijf, 2014). EBSD quite often can miss much of the small RA grains that XRD does not, causing it to show a smaller percentage than expected; this can also be aggravated by mis-indexing of the phases, as discussed in the previous section. Second, because the samples had to be mechanically polished, it is suspected that some of the austenite transformed due to the strains caused during the polishing steps (Ennis, 2017). Finally, the scan areas typically incorporated the fiducials made with the FIB. This is important

to note because it has been found that the ions used to mill the surface also cause RA transformation of the area being milled (Babu, 2016; Basa, 2014; Knipling, 2010). Unfortunately, it was necessary to scan around the fiducials to enable DIC and better tracking of grains. It is not known, however, how much of the RA in the vicinity of the fiducials had transformed previous to EBSD scanning, which means that the reported RA percentages could easily lower than expected. A summary of this analysis is shown in Table 3 but should be noted that it represents a single scan at each distance. Future effort will be directed at confirming these initial results.

Table 3 Austenite Percentage at Different Distances Away From FIB Mark

	No cleanup	CI >.05 Cleanup
Around FIB marking	0.089	0.049
50 micron away	0.088	0.055
100 micron away	0.111	0.072

Additionally, as mentioned earlier, carbon deposition on the scan area increased each time the area was scanned, which causes a decrease in scan quality. While confidence index values were used to determine how accurately a pattern was indexed, as pattern quality became worse, indexing them was too difficult to determine any phase at all. Therefore, as the scans progressed to each strain increment and the overall pattern quality decreased, some of the phase content was lost. This could easily explain why the austenite percentage continued to decrease for the in situ samples when compared to the ex-situ Instron samples which were scanned only once, removing the problem of carbon buildup.

To help solve the problem of determining how much the reported transformation that occurred was due to carbon deposition, the samples were lightly polished, after being strained, with 0.01um colloidal silica for approximately 60 seconds to remove the carbon layer over the scan areas. The sample was then scanned again and close to the original scan quality was obtained (see Figure 21). The resulting austenite reported from the same scan area was 1.7% after removing low CI points, which lines up quite well with the final percentage of the ex-situ sample.
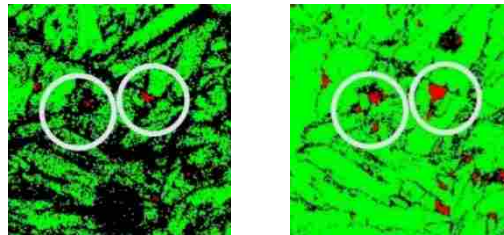

Fig 21-Scan Area at 14% Macro Strain Before & After Removing Carbon Layer

4.3   Forming Limits of Q&P 1180

Experimental strain paths were measured using DIC on sheets that were stretched under biaxial tension, plane-strain tension, and uniaxial tension. Plots of the strain paths, and associated DIC strain maps just before necking (left image) and just before fracture (right image), are shown in Figure 22-24 for each case.

The plots show that biaxial tension and uniaxial tension strain paths are consistent. For plane-strain tension, the initial strains are slightly positive biaxial, then tend toward plane strain, then later become a bit more uniaxial in nature. But all of these plots have terminal strains that are much greater than the "limit" strain of the material, because they include strain values that occur after necking.
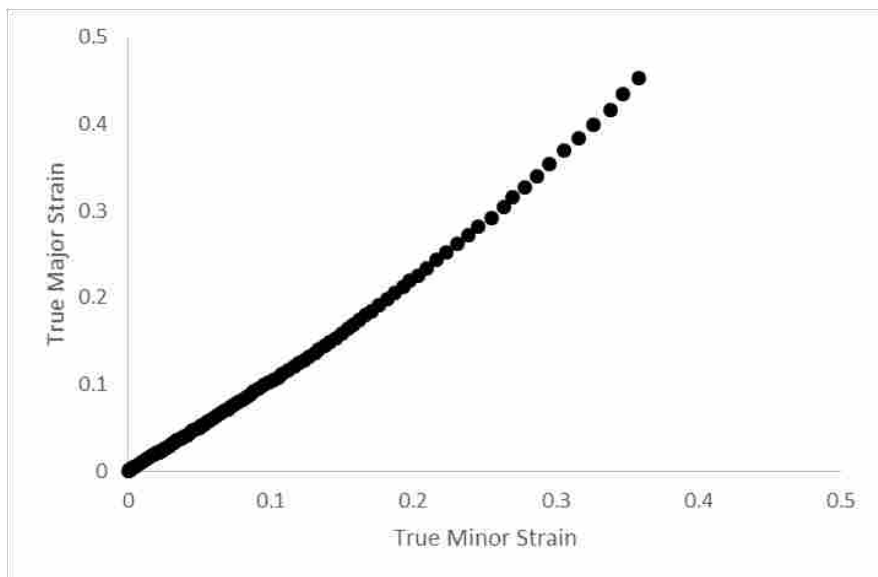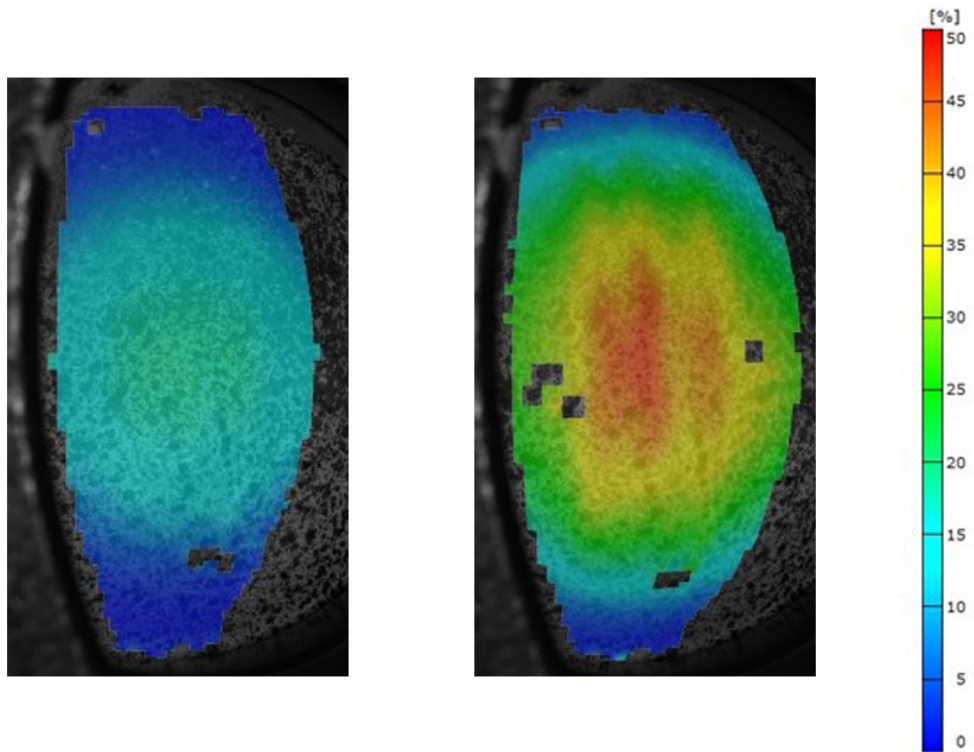
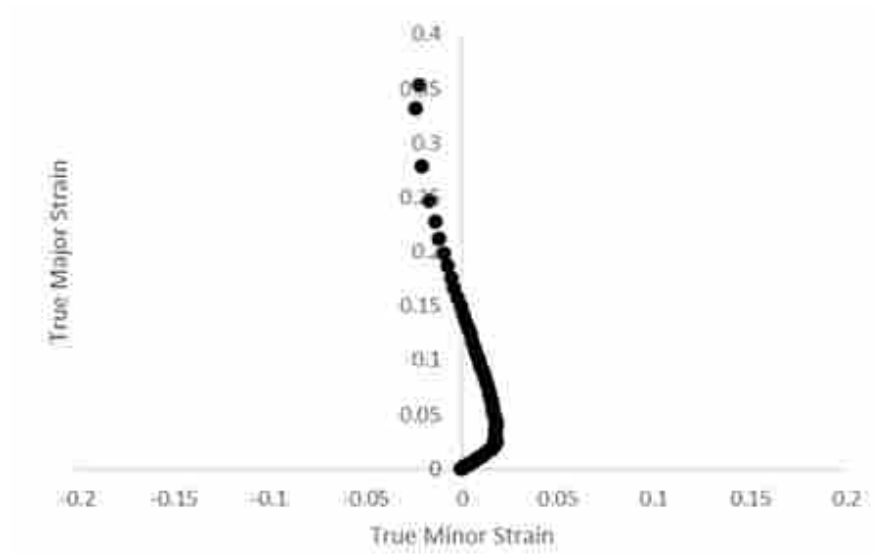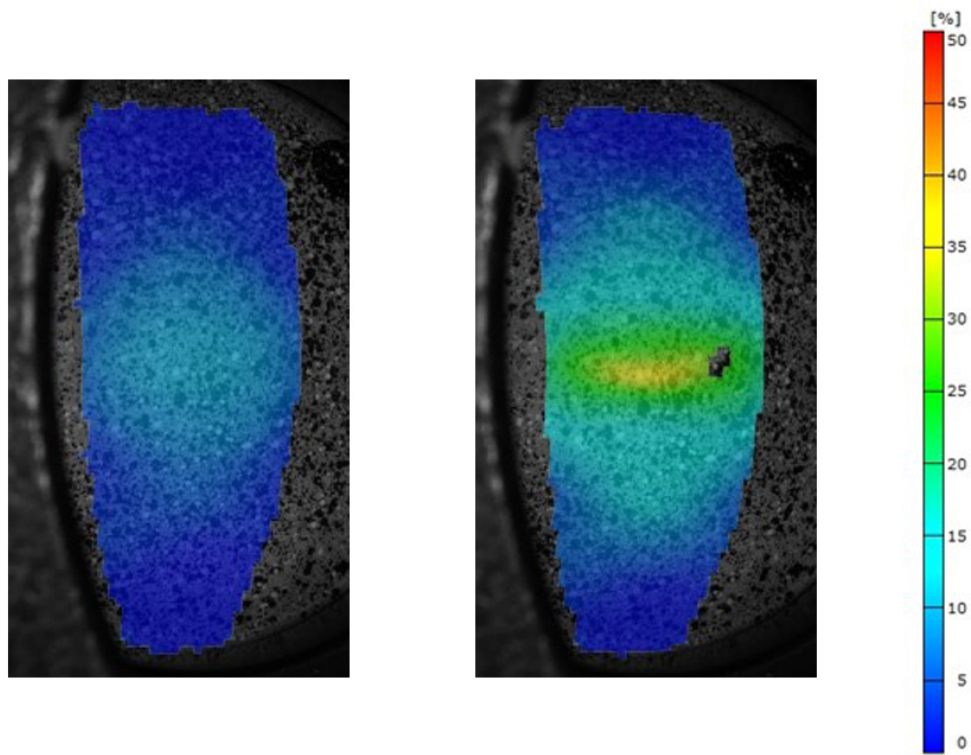Fig 22-Strain Path from DIC Measurements for Biaxial Tension Specimen

Fig 23-Strain Path from DIC Measurements for Plane-Strain Specimen
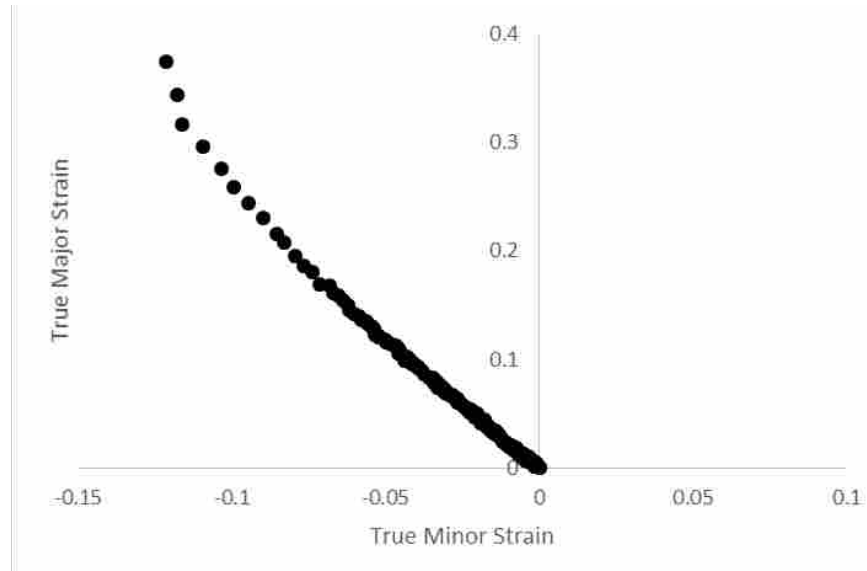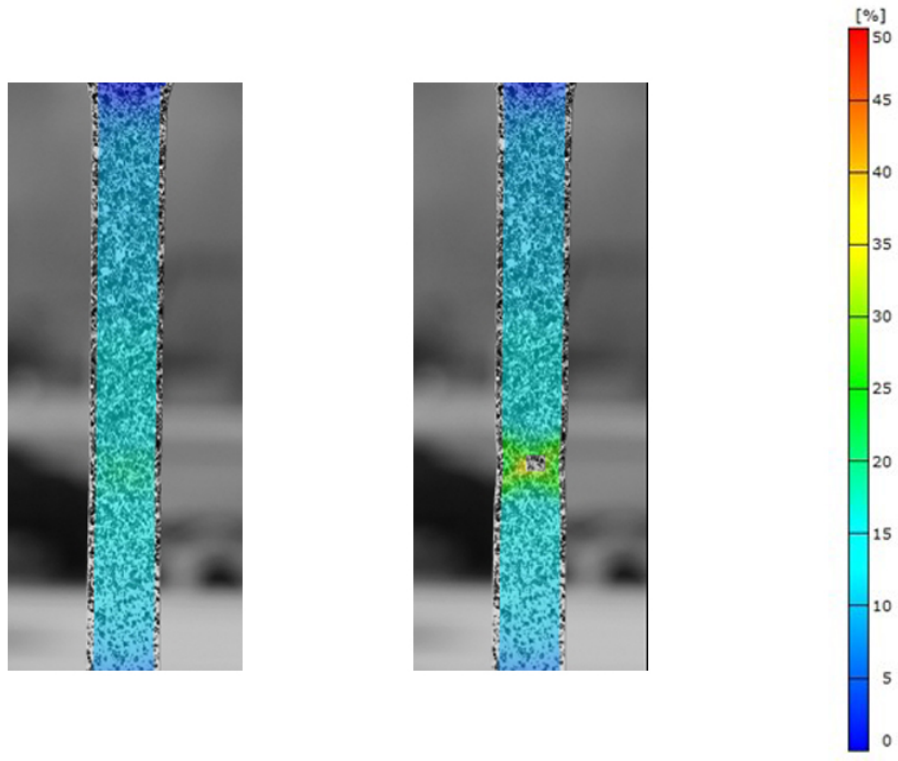
Fig 24-Strain Paths from DIC Measurements Uniaxial Tension Specimen.

To determine the true limit strains from the DIC strain data, the strain rate was computed at the eventual fracture location, for all of the data from each test, using the following approach:

$$\dot{\varepsilon}_1\,(j) = \frac{d\varepsilon_1}{dt} \approx \frac{\varepsilon_1\,(j+1) - \varepsilon_1\,(j-1)}{2\tau} \qquad (1)$$

where $\dot{\varepsilon}_1$ is the strain rate in the major direction, ε_1 is true strain in the major direction, τ is the period between frames, and j is the frame number from the DIC analysis (Min, 2017). In this case, the period between frames was approximately 1 second. Plots of strain rate vs time for each strain path are shown in Figure 25-27.
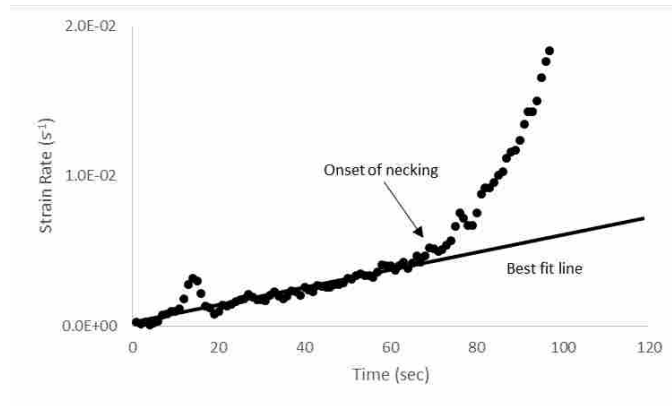
Fig 25-Strain Rate for Biaxial Tension to Identify Onset of Necking
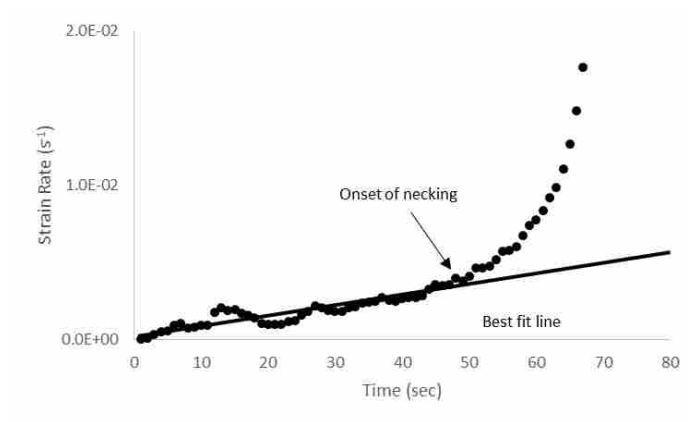
Fig 26-Strain Rate for Plane-Strain Tension to Identify Onset of Necking
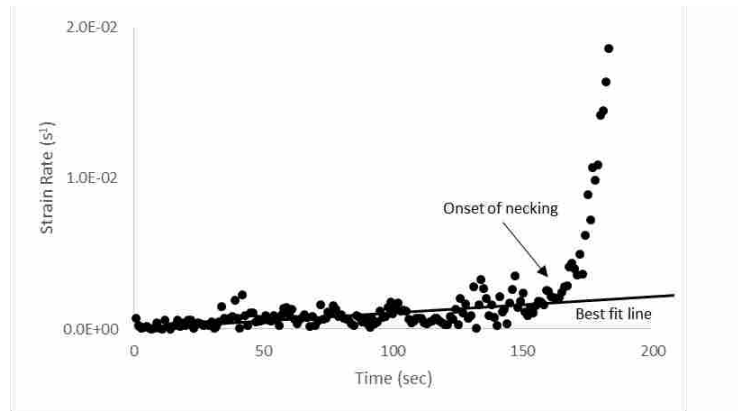
Fig 27-Strain Rate for Uniaxial Tension to Identify Onset of Necking

When the strain rate increases rapidly and diverges from a best-fit line of the linear portion of the curve, then the onset of necking is considered to have occurred (for the strain rate of the jth frame at the point of divergence). The corresponding true major strain at the jth frame is then taken as the limit strain for the material, for the particular strain path imposed. Using these limit strains, along with the strains measured for various increments of stretching along each strain path, the forming limit curve was generated for 1.2mm Q&P 1180, as shown in Figure 28. Each data point represents a specimen, and each path required 4 specimens
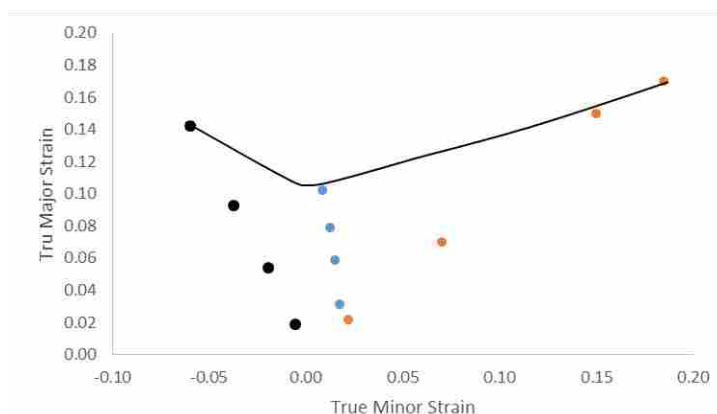
Fig 28-Forming Limit Diagram for Q&P 1180 With Corresponding Strain Paths

After the stretching experiments were completed, specimens were cut from the sheets and mounted for EBSD analysis. Percent retained austenite was measured by EBSD as a function effective strain. Three measurements of retained austenite were performed for each strain level, as can be seen in Figure 29-31. In this case, the three measurements were not on separate specimens. Each strain level had three separate scans in different areas on the surface of each specimen.
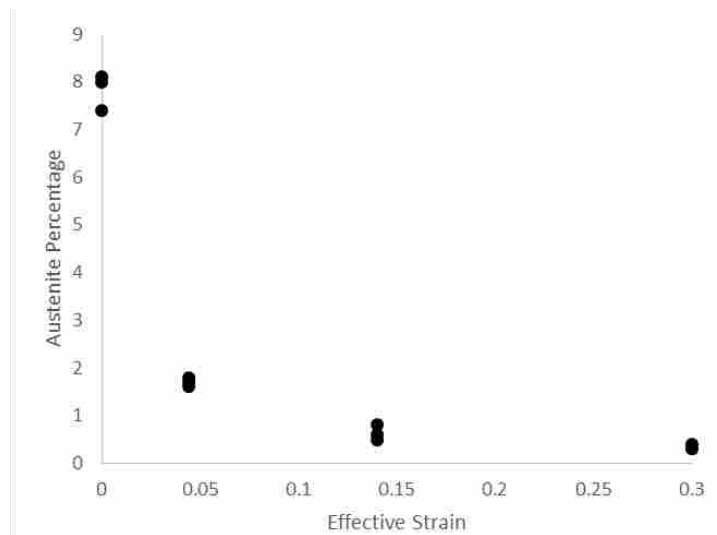
Fig 29-Percent RA as a Function of Effective Strain for Biaxial Tension
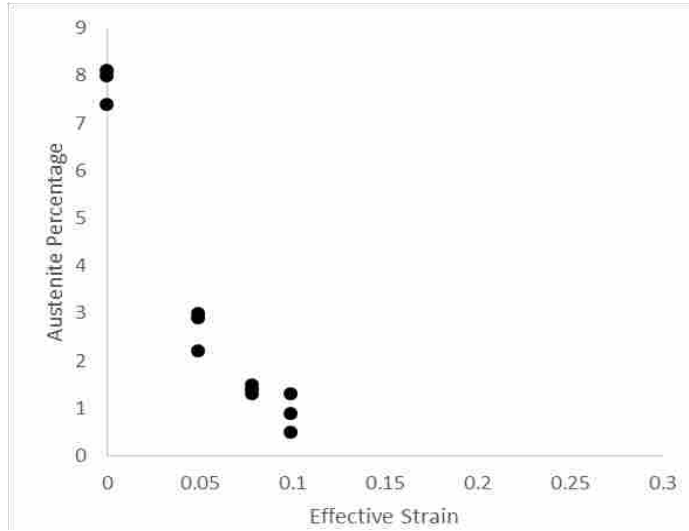
Fig 30-Percent RA as a Function of Effective Strain for Plane-Strain Tension
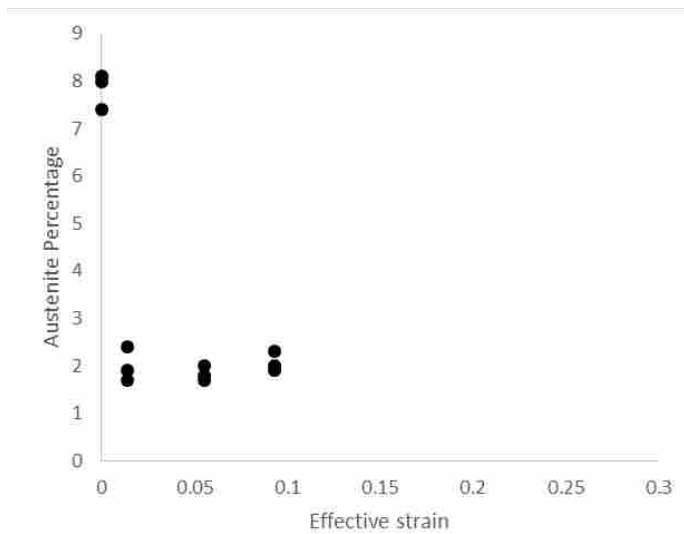
Fig 31-Percent RA as a Function of Effective Strain for Uniaxial Tension

4.4 Strain Path Effect on Austenite Transformation

DIC strains were measured for each specimen, resulting in the FLD shown in Figure 28.

Because the limit strains were different for each strain path, the plots in Figure 29-31 reflect this.

For example, the biaxial tension case exhibited the highest level of strain at fracture, and the

corresponding strain increments for the 25%, 50%, and 75% displacements are associated with higher strain levels than the plane-strain or uniaxial tension cases (hence the reason for different strain levels on the plots). For biaxial tension, it appears that most of the retained austenite was converted to martensite in the first strain increment, dropping from about 8% (volume fraction) in the base material to about 2% in the specimen deformed to an effective strain of 0.05 (Figure 29). For the plane-strain case, the first strain increment dropped the retained austenite content to between 2 and 3% (Figure 30). And for uniaxial tension, the first strain increment resulted in a retained austenite content of about 2% (Figure 31). However, for greater levels of strain beyond the first increment, the retained austenite levels continued to drop in both the biaxial and plane-strain tension cases, but not in the uniaxial tension case. In the latter case it appears that the conversion of austenite to martensite saturated at the first strain increment. The biaxial tension case appears to be the most "effective" in the conversion of retained austenite, dropping to about 0.3% in the third strain increment, compared to about 0.9% for plane-strain tension and about 2% for uniaxial tension. The corresponding thinning strains for this last strain increment were -0.36 for biaxial tension, -0.11 for plane-strain tension, and -0.082 for uniaxial tension. Thinning combined with in-plane stretching appears to convert austenite more completely in the biaxial case than in the other two cases; this may be contributing to the greater level formability seen in the biaxial tension case compared to plane strain tension, or even uniaxial tension.

5   CONCLUSIONS

5.1   Summary

The intent of this research has been to study the effect of strain level and strain path on austenite transformation in a 1.2mm thick Q&P 1180 steel sheet material.

The data provide evidence to confirm both of the hypotheses that were posed: transformation of RA is a non-linear function of strain, with the bulk of the austenite transforming to martensite during the first small increments of deformation. For example, in the uniaxial tension virtually all of the conversion happened after an effective strain of just 0.02. In biaxial tension and plane strain tension the bulk of the conversion happened after an effective strain of 0.05, but then additional transformation occurred at a slower rate with increasing strain. While another material was not studied for comparison, it is likely that conversion rate is affected by phase morphology and chemistry. Perhaps it would be beneficial if a microstructure could be designed to promote a more even conversion of austenite with strain level.

When comparing the current results with those of Speer, discussed in section 4, the general trend of the transformation is similar. Therefore, this study confirms the findings presented in Speer's study. However, in addition to simply confirming the previous study, the current study also displays the capability of EBSD with regards to in situ phase tracking. While XRD can return accurate phase contents, it cannot report on local phase and microstructure, both

of which are available through EBSD. Furthermore, EBSD allows for easy addition of FSD scans that can be used to compute local strain paths.

In terms of forming limits under different strain paths, biaxial tension was the most "effective" at transforming retained austenite to martensite as the sheets were stretched to failure. Plane strain was slightly less effective, but the rate of transformation was greatest for this case, which is consistent with its limit strain being the lowest of the three strain paths. Uniaxial tension was the least effective, which can be correlated with thinning strains. The three strain paths are rank ordered in the following way with respect to thinning strain near failure: biaxial tension > plane strain tension > uniaxial tension. Uniaxial tension provides the least restraint, with respect to forming boundary conditions, because it can freely deform along the major strain direction, while contracting in the minor strain and thickness strain directions. Having the ability to contract in the minor strain direction delays thinning strains until fracture occurs. In other words, it isn't possible to achieve a uniform thinning strain in uniaxial tension as low as the ones that were seen in biaxial or plane strain tension. Therefore, it appears that the strain paths that maximize thinning strains during uniform straining are the ones that result in the greatest levels of austenite conversion. This observation will likely be important as other morphologies and chemistries are studied in steels containing retained austenite, and then compared to steels without it, because not all steels have greater limit strains in biaxial tension than in uniaxial tension. The efficiency of conversion of retained austenite may partly explain the high level of biaxial tension formability in Q&P 1180.

5.2 Recommendations

The FIB, used to mark the samples to line up each scan after every pull and for better tracking in DIC software, causes transformation of retained austenite in the region of interest. Further work should be done in developing a method in which lining up each scan after each pull does not involve microindenting or fibbing of the sample.

There are a number of testing and analysis methods that might be employed which were outside the scope of this study. Various microstructures affect the mechanical properties of the material; therefore, understanding the microstructural characteristics is useful in optimizing the steel's mechanical properties. The deformation stability of RA in TRIP steels is influenced by following factors: (i) the grain size of RA; (ii) the local carbon content in RA ; (iii) the morphology; (iv) the crystallographic orientation of RA relevant to the loading direction; and (v) the constraining effect exerted by surrounding phases on RA. (Li, 2016) Researching these different factors and how they affect RA transformation in Q&P steels will help in further optimizing the formability of this material.

REFERENCES

Babu, R. P., Irukuvarghula, S., Harte, A., & Preuss, M. (2016). Nature of gallium focused ion beam induced phase transformation in 316L austenitic stainless steel. *Acta Materialia, 120*(Supplement C), 391-402. doi:https://doi.org/10.1016/j.actamat.2016.08.008

Basa, A., Thaulow, C., & Barnoush, A. (2014). Chemically Induced Phase Transformation in Austenite by Focused Ion Beam. *Metallurgical and Materials Transactions A, 45*(3), 1189-1198. doi:10.1007/s11661-013-2101-4

Bhadeshia, H. K. D. H. (2002). TRIP-Assisted Steels? *ISIJ International, 42*(9), 1059-1060. doi:10.2355/isijinternational.42.1059

Blaber, J., Adair, B., & Antoniou, A. (2015). Ncorr: Open-Source 2D Digital Image Correlation Matlab Software. *Experimental Mechanics, 55*(6), 1105-1122. doi:10.1007/s11340-015-0009-1

Blondé, R., Jimenez-Melero, E., Zhao, L., Wright, J. P., Brück, E., van der Zwaag, S., & van Dijk, N. H. (2012). High-energy X-ray diffraction study on the temperature-dependent mechanical stability of retained austenite in low-alloyed TRIP steels. *Acta Materialia, 60*(2), 565-577. doi:https://doi.org/10.1016/j.actamat.2011.10.019

Cakmak, E., Choo, H., Kang, J.-Y., & Ren, Y. (2015). Relationships Between the Phase Transformation Kinetics, Texture Evolution, and Microstructure Development in a 304L Stainless Steel Under Biaxial Loading Conditions: Synchrotron X-ray and Electron Backscatter Diffraction Studies. *Metallurgical and Materials Transactions A, 46*(5), 1860-1877. doi:10.1007/s11661-015-2772-0

Choi, K. S., Liu, W. N., Sun, X., Khaleel, M. A., & Fekete, J. (2009). Influence of manufacturing processes and microstructures on the performance and manufacturability of advanced high strength steels. *Journal of Engineering Materials and Technology, 131*(4), 041205.

Choi, S. H., Kim, E. Y., & Kim, S. I. (2014). The micromechanical deformation behaviors of hot-rolled 590FB steel during hole-expansion test. *International Journal of Plasticity, 58*(Supplement C), 184-200. doi:https://doi.org/10.1016/j.ijplas.2013.11.010

Clarke, A. J., Speer, J. G., Miller, M. K., Hackenberg, R. E., Edmonds, D. V., Matlock, D. K., . . . De Moor, E. (2008). Carbon partitioning to austenite from martensite or bainite during the quench and partition (Q&P) process: A critical assessment. *Acta Materialia, 56*(1), 16-22. doi:http://dx.doi.org/10.1016/j.actamat.2007.08.051

de Diego-Calderón, I., Sabirov, I., Molina-Aldareguia, J. M., Föjer, C., Thiessen, R., & Petrov, R. H. (2016). Microstructural design in quenched and partitioned (Q&P) steels to improve their fracture properties. *Materials Science and Engineering: A, 657*(Supplement C), 136-146. doi:https://doi.org/10.1016/j.msea.2016.01.011

De Knijf, D., Föjer, C., Kestens, L. A., & Petrov, R. (2015). Factors influencing the austenite stability during tensile testing of Quenching and Partitioning steel determined via in-situ Electron Backscatter Diffraction. *Materials Science and Engineering: A, 638*, 219-227.

De Knijf, D., Petrov, R., Föjer, C., & Kestens, L. A. I. (2014). Effect of fresh martensite on the stability of retained austenite in quenching and partitioning steel. *Materials Science and Engineering: A, 615*(Supplement C), 107-115. doi:https://doi.org/10.1016/j.msea.2014.07.054

De Moor, E., Lacroix, S., Clarke, A. J., Penning, J., & Speer, J. G. (2008). Effect of Retained Austenite Stabilized via Quench and Partitioning on the Strain Hardening of Martensitic Steels. *Metallurgical and Materials Transactions A, 39*(11), 2586. doi:10.1007/s11661-008-9609-z

Di Gioacchino, F., & da Fonseca, J. Q. (2013). Plastic strain mapping with sub-micron resolution using digital image correlation. *Experimental Mechanics, 53*(5), 743-754.

Edmonds, D., He, K., Rizzo, F., De Cooman, B., Matlock, D., & Speer, J. (2006). Quenching and partitioning martensite—A novel steel heat treatment. *Materials Science and Engineering: A, 438*, 25-34.

Ennis, B. L., Jimenez-Melero, E., Atzema, E. H., Krugla, M., Azeem, M. A., Rowley, D., . . . Lee, P. D. (2017). Metastable austenite driven work-hardening behaviour in a TRIP-assisted dual phase steel. *International Journal of Plasticity, 88*(Supplement C), 126-139. doi:https://doi.org/10.1016/j.ijplas.2016.10.005

Grajcar, A., Kuziak, R., & Zalecki, W. (2012). Third generation of AHSS with increased fraction of retained austenite for the automotive industry. *Archives of civil and mechanical engineering, 12*(3), 334-341.

Handbook, ASM. (2006). Volume 14B Metalworking: Sheet Forming. *ASM International, 924*.

Kimura, T. (2011). Formability of TRIP Type Bainitic Ferrite Steel Sheet. *Kobelco Technology Review, 30*, 5.

Knipling, K. E., Rowenhorst, D. J., Fonda, R. W., & Spanos, G. (2010). Effects of focused ion beam milling on austenite stability in ferrous alloys. *Materials Characterization, 61*(1), 1-6. doi:https://doi.org/10.1016/j.matchar.2009.09.013

Krauss, G. (2015). *Steels: processing, structure, and performance*: Asm International.

Kuziak, R., Kawalla, R., & Waengler, S. (2008). Advanced high strength steels for automotive industry. *Archives of civil and mechanical engineering, 8*(2), 103-117. doi:http://dx.doi.org/10.1016/S1644-9665(12)60197-6

Kwon, O., Lee, K. Y., Kim, G. S., & Chin, K. G. (2010). *New trends in advanced high strength steel developments for automotive application.* Paper presented at the Materials Science Forum.

Li, W.-s., Gao, H.-y., Nakashima, H., Hata, S., & Tian, W.-h. (2016). In-situ EBSD study of deformation behavior of retained austenite in a low-carbon quenching and partitioning steel via uniaxial tensile tests. *Materials Characterization, 118*, 431-437.

Min, J., Stoughton, T. B., Carsley, J. E., & Lin, J. (2017). Comparison of DIC Methods of Determining Forming Limit Strains. *Procedia Manufacturing, 7*(Supplement C), 668-674. doi:https://doi.org/10.1016/j.promfg.2016.12.099

Miura, M., Nakaya, M., & Mukai, Y. (2008). Cold-rolled, 980MPa Grade Steel Sheets with Excellent Elongation and Stretch Flangeability. *Kobelco Technology Review, 28*, 5.

OIM. (2016). OIM Analysis 8 Reference Manual.

Sadagopan, S., & Urban, D. (2003). *Formability Characterization of a New Generation of High Strength Steels*. Retrieved from Pittsburgh, PA 15222:

Santofimia, M. J., Zhao, L., & Sietsma, J. (2011). Overview of Mechanisms Involved During the Quenching and Partitioning Process in Steels. *Metallurgical and Materials Transactions A, 42*(12), 3620. doi:10.1007/s11661-011-0706-z

Shaw, J. R., & Zuidema, B. K. (2001). *New High Strength Steels Help Automakers Reach Future Goals for Safety, Affordability, Fuel Efficiency and Environmental Responsibility*. http://doi.org/10.4271/2001-01-3041

Speer, J. G., Assunção, F. C. R., Matlock, D. K., & Edmonds, D. V. (2005). The" quenching and partitioning" process: background and recent progress. *Materials Research, 8*(4), 417-423.

Speer, J. G., Matlock, D. K., Wang, L., & Edmonds, D. V. (2014). 1.11 - Quenched and Partitioned Steels A2 - Hashmi, Saleem. In G. F. Batalha, C. J. V. Tyne, & B. Yilbas (Eds.), *Comprehensive Materials Processing* (pp. 217-225). Oxford: Elsevier.

Systems, T. O. T. (2011). "Aramis 3D DIgital Image Correlation Strain & 3D Deformation,".

Wang, L., & Speer, J. G. (2013). Quenching and Partitioning Steel Heat Treatment. *Metallography, Microstructure, and Analysis, 2*(4), 268-281. doi:10.1007/s13632-013-0082-8

WorldAutoSteel. (2017). Advanced High Strength Steel Application Guidelines. In (Vol. Version 6).